PHYSICAL REVIEW B **85**, 174110 (2012)

# Crystal structures, strain analysis, and physical properties of $Sr_{0.7}Ce_{0.3}MnO_3$

Zhaoming Zhang,[1,*] Brendan J. Kennedy,[2] Christopher J. Howard,[3] Michael A. Carpenter,[4] Wojciech Miiller,[1,2]
Kevin S. Knight,[5] Motohide Matsuda,[6] and Michihiro Miyake[7]
[1]*Australian Nuclear Science and Technology Organisation, Locked Bag 2001, Kirrawee DC, NSW 2232, Australia*
[2]*School of Chemistry, The University of Sydney, Sydney, NSW 2006, Australia*
[3]*School of Physics, The University of Sydney, Sydney, NSW 2006, Australia*
[4]*Department of Earth Sciences, University of Cambridge, Cambridge, CB2 3EQ, United Kingdom*
[5]*ISIS Facility, Rutherford Appleton Laboratory, Chilton, Didcot, OX11 0QX, United Kingdom*
[6]*Department of Materials Science and Engineering, Faculty of Engineering, Kumamoto University, 2-39-1 Kurokami, Kumamoto 860-8555, Japan*
[7]*Graduate School of Environmental Science, Okayama University, 3-1-1 Tsushima-Naka, Okayama 700-8530, Japan*

(Received 4 January 2012; revised manuscript received 8 March 2012; published 24 May 2012)

We have studied the crystal structure of mixed-valence $Sr_{0.7}Ce_{0.3}MnO_3$ from 4.2 to 973 K using high-resolution neutron powder diffraction. The crystal structure is tetragonal in space group $I4/mcm$ at 4.2–923 K and cubic in $Pm\bar{3}m$ at T $\geqslant$ 948 K. Lattice parameters and Mn-O bond distances, obtained by Rietveld refinement, have been used to derive the spontaneous strains and $MnO_6$ octahedral distortion, which are interpreted in terms of strain/order parameter coupling using a single Landau free-energy expansion for a $Pm\bar{3}m$ reference structure with two instabilities ($R_4^+$ and $\Gamma_3^+$). Two phase transitions were proposed: an octahedral tilting transition at $T_{c,\phi} \sim 938$ K ($Pm\bar{3}m \leftrightarrow I4/mcm$, $R_4^+$), and an isosymmetric, electronically driven (Jahn-Teller–like) transition at $T_{c,JT} \sim 770$ K ($I4/mcm$, $R_4^+ \leftrightarrow I4/mcm$, $R_4^+$ and $\Gamma_3^+$). The nature of the tilting transition appears to be tricritical, while that of the Jahn-Teller–like transition is second order. In addition to the contributions from octahedral tilting and Jahn-Teller–like distortions, there is an excess octahedral distortion at temperatures below 250 K; this is speculated to be associated with an anomaly observed over the temperature range of 275–300 K in the heat-capacity measurements.

DOI: 10.1103/PhysRevB.85.174110 PACS number(s): 61.05.fm, 61.50.Ks, 64.60.Ej

## I. INTRODUCTION

There has been an extensive number of studies on the perovskite-type manganites in recent years, owing to the discovery of colossal magnetoresistance (CMR) in hole-doped manganites $Ln_{1-x}A_xMnO_3$ with mixed $Mn^{3+}/Mn^{4+}$ ions ($Ln$ = trivalent lanthanoid and $A$ = divalent alkaline-earth ions such as Ca and Sr).[1–3] The fascinating physical properties displayed by this class of materials are largely attributed to the strong interactions among the crystal, magnetic, and electronic structures.[4]

In contrast to hole-doped ($Mn^{3+}$-rich) manganites, electron-doped materials $A_{1-x}Ln_xMnO_3$ ($Mn^{4+}$-rich) have received less attention. $Sr_{1-x}Ce_xMnO_3$ is one of the more interesting electron-doped manganite series. Pure $SrMnO_3$ has a four-layer hexagonal structure at temperatures below 1035 °C (although metastable cubic $SrMnO_3$ can be obtained by reoxidizing anion-deficient perovskite phases).[5] The substitution of a small amount of Ce for Sr can stabilize the archetypal cubic perovskite structure, e.g., in polycrystalline $Sr_{0.95}Ce_{0.05}MnO_3$[6] and $Sr_{0.925}Ce_{0.075}MnO_3$.[7] To maintain charge neutrality upon partial replacement of Sr by Ce, some of the $Mn^{4+}$ ions are reduced to $Mn^{3+}$, introducing Jahn-Teller (JT)–active $Mn^{3+}$ ($d^4$) ions. This brings about a transition to a tetragonal structure, due to the cooperative Jahn-Teller distortions, at $x \sim 0.1$ for polycrystalline $Sr_{1-x}Ce_xMnO_3$[7,8] or $x \sim 0.02$ for single crystals.[9] However, as the Ce and, hence, Jahn-Teller–active $Mn^{3+}$ content increases further, the distortion of the cell metric (i.e., $c/a$ ratio) decreases while the $MnO_6$ octahedral tilt angle increases until an orthorhombic structure forms at $x \sim 0.35$.[7] This apparent disjoint between the cell metric and internal distortion appears to be associated with the reduction in the coherence of the orbital ordering.[10] X-ray absorption near edge structure (XANES) measurements at the Mn K-edge[10] have confirmed the partial reduction of $Mn^{4+}$ to $Mn^{3+}$ in $Sr_{1-x}Ce_xMnO_3$, although the amount of $Mn^{3+}$ does not increase linearly with the Ce content, discounting previously proposed charge compensation models of one $Ce^{3+}$ for one $Mn^{3+}$ or one $Ce^{4+}$ for two $Mn^{3+}$ throughout the series.[8,11] The Ce L-edge XANES results are in excellent agreement with those from the Mn K-edge measurements,[10] indicating that Ce ions in $Sr_{1-x}Ce_xMnO_3$ are in a tetravalent state for $x < 0.2$, but mixed $Ce^{3+}$ and $Ce^{4+}$ for $x \geqslant 0.2$ (in contrast to $Ca_{1-x}Ce_xMnO_3$,[10,12] in which the Ce valency remains 4+); the presence of $Ce^{3+}$ ions is believed to be necessary in order to reduce the $A$-site cation disorder.[10] According to XANES results, proportions are approximately 50% $Mn^{3+}$/50% $Mn^{4+}$ and 30% $Ce^{3+}$/70% $Ce^{4+}$ in $Sr_{0.7}Ce_{0.3}MnO_3$.[10]

A recent study on single-crystal $Sr_{1-x}Ce_xMnO_3$ ($0 \leqslant x \leqslant 0.1$)[9] revealed that undoped cubic (metastable) $SrMnO_3$ is an insulator, with a transition from a paramagnetic (PM) phase to a G-type antiferromagnetic (G-AFM) phase at a Neel temperature ($T_N$) around 231 K. The system becomes an AFM metal with only 0.5–1% of Ce-doping ($T_N \sim 220$ K).[9] Upon further increase in the Ce content ($x > 0.02$), the metallic ground state is replaced by an insulator with tetragonal lattice distortion (i.e., accompanied by orbital ordering) and a C-type antiferromagnetic (C-AFM) phase.[9] Earlier studies on polycrystalline $Sr_{1-x}Ce_xMnO_3$[8,13,14] also reported $Sr_{0.9}Ce_{0.1}MnO_3$ having a C-AFM ground state, and the dilution of antiferromagnetic interaction at higher Ce content, which results in a spin-glass–like behavior at low temperatures. Another study by Mandal *et al.*,[11] however, did not report any long-range magnetic ordering for samples with $x \geqslant 0.1$, only spin-glass–like behavior at low temperatures and charge ordering for samples with $x \geqslant 0.15$. It should be mentioned that the orthorhombic structure reported by Mandal *et al.*[11] for samples with $0.1 \leqslant x \leqslant 0.3$ is also different from the tetragonal structure reported in the other studies[8,13,14]; these differences may be attributed to the use of different sample preparation methods.[11]

It is well known that lattice parameters obtained from Rietveld refinements can be used to derive spontaneous strains.[15–19] Such strains arising at phase transitions are expected to provide detailed insights into the nature and mechanisms of the phase transitions.[20,21] In the present work, we determined the crystal structures of $Sr_{0.7}Ce_{0.3}MnO_3$ from 4.2 to 973 K using high-resolution neutron powder diffraction, and we converted the resulting high-precision lattice parameters to symmetry-adapted strains in order to follow the evolution of strain/order parameter coupling for combined "Jahn-Teller" and octahedral tilting transitions. Note that herein we use inverted commas to signify that we postulate a change in electronic structure as being responsible for distortions that are additional to the effects of octahedral tilting, though the situation is not quite that of a normal Jahn-Teller transition. Direct current (DC) magnetic susceptibility, magnetization, and heat capacity were also measured. The objective of this work is to better understand the interplay among the structural, magnetic, and electronic properties of electron-doped manganites $Sr_{1-x}Ce_xMnO_3$.

## II. EXPERIMENTAL METHODS

The polycrystalline $Sr_{0.7}Ce_{0.3}MnO_3$ sample was prepared by standard solid-state reaction methods. Powders of $SrCO_3$ (Kanto Kagaku, 99.9%), $CeO_2$ (Kanto Kagaku, 99.99%), and $Mn_3O_4$ (Kojundo Kagaku, 99.9%) were weighed at stoichiometric proportions and mixed for 24 h using a ball mill. The mixture was calcined at 800 °C for 10 h in air. The calcined powder was then crushed in a ball mill for 24 h, sintered at 1400 °C for 10 h in air, and furnace cooled to room temperature. The crystallinity and phase purity of the sample were checked using laboratory powder X-ray diffraction with Cu $K_\alpha$ radiation. The sample was also analyzed using a JEOL 6400 scanning electron microscope fitted with an energy dispersive spectrometer. This verified the sample composition and showed it to be a homogeneous solid solution.

Time-of-flight powder neutron diffraction data were recorded using the high-resolution powder diffractometer (HRPD) at the ISIS neutron facility, Rutherford Appleton Laboratories, UK.[22] The temperature range of interest, from 4.2 to 973 K, necessitated the use of both cryostat and furnace. The powdered sample of $Sr_{0.7}Ce_{0.3}MnO_3$ was lightly packed into either an aluminum can of slab geometry for measurements in the cryostat (4.2–373 K), or a thin-walled 11-mm-diameter vanadium can for analysis in the furnace (first at room temperature, followed by measurements from 373 to 973 K). Details of the cryostat and furnace have been reported previously.[23] Diffraction patterns from the sample, whether in cryostat or furnace, were recorded over the time-of-flight range 30–130 ms in both back-scattering and ninety-degree detector banks, corresponding to $d$-spacings from 0.6 to 2.6 Å (at a resolution $\Delta d/d \sim 4 \times 10^{-4}$) and from 0.9 to 3.7 Å ($\Delta d/d \sim 2 \times 10^{-3}$), respectively (independent of $d$). The patterns were normalized to the incident beam spectrum as recorded in the upstream monitor, and corrected for detector efficiency according to prior calibration with a vanadium scan. Patterns collected inside the furnace were recorded to a total incident proton beam of 10 $\mu$A h (corresponding to approximately 20 min of data collection), sufficient to give a good determination of lattice parameters and reasonable estimates of internal coordinates. Most patterns collected inside the cryostat were recorded to a total incident proton beam of 8 $\mu$A h, but longer counting exposures were employed at 4.2 K (22 $\mu$A h) and 373 K (95 $\mu$A h).

The neutron diffraction patterns, from the back-scattering and the ninety-degree detector banks, were fitted simultaneously, using the Rietveld method[24] as implemented in the GSAS computer program.[25,26] The diffractometer constant for the ninety-degree bank was released to ensure that the lattice parameters were determined by the higher-resolution back-scattering bank in every case. The diffractometer constants used in the furnace run were slightly adjusted so that the lattice parameters obtained in the furnace matched those obtained in the cryostat in the overlapping temperature range. Such an adjustment is justified on the grounds that the diffractometer constants depend on the precise positioning of the sample, which could be different in the furnace as compared with that in the cryostat. The peak shapes were modeled as convolutions of back-to-back exponentials with a pseudo-Voigt, in which two peak width parameters were varied, and the background was modeled as Chebyshev polynomials.[25] Atomic displacement parameters (ADP) were refined along with internal coordinates, and the oxygen displacement parameters were taken to be anisotropic except at $T \geqslant 753$ K (in order to avoid physically unreasonable ADP for O1). The isotropic displacement parameters for the two $A$-site cations (Sr and Ce) were constrained to be equal.

DC susceptibility measurements were performed at 0.5 T magnetic field under field-cooling (FC) and zero-field-cooling (ZFC) conditions over the temperature range 2–390 K. A field dependence of magnetization, $M(B)$, was collected at selected temperatures in magnetic fields up to 9 T. Heat-capacity measurements were carried out over the temperature range 2.6–320 K employing the thermal relaxation method. All physical properties were collected using a Quantum Design physical properties measurement system (PPMS).

## III. RESULTS AND DISCUSSIONS

### A. Structure refinements and strain analysis

Different phases were identified by close inspection of the diffraction patterns, paying particular attention to the splitting of the Bragg reflections as well as the presence of superlattice reflections associated with the tilting of the $MnO_6$ octahedra. It was found that the structure of $Sr_{0.7}Ce_{0.3}MnO_3$ is tetragonal in space group $I4/mcm$ (tilt system $a^0a^0c^-$ in Glazer's notation[27]) at 4.2–923 K, and cubic in space group $Pm\bar{3}m$

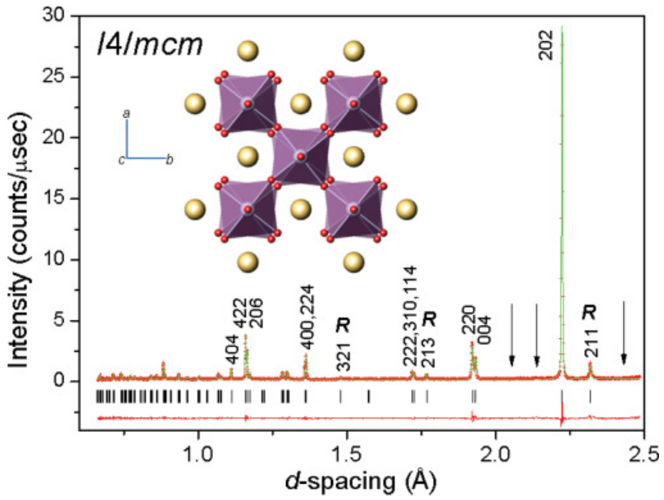

FIG. 1. (Color online) Neutron diffraction pattern recorded at 4.2 K from $Sr_{0.7}Ce_{0.3}MnO_3$. The crosses represent the observed data, and the continuous line is the fit obtained by the Rietveld method using the tetragonal structure in $I4/mcm$. The vertical marks show the peak positions expected in this structure, and the line beneath the pattern records the difference between the observed and calculated patterns. $R$-point reflections are associated with out-of-phase tilting of the $MnO_6$ octahedra. Arrows indicate where magnetic peaks are expected based on a C-type antiferromagnetic structure, as reported for $Sr_{0.9}Ce_{0.1}MnO_3$.[8] The inset shows the perspective view along the $c$-axis of the structure, as prepared using the computer program *ATOMS* (Shape Software, 2003).

$(a^0a^0a^0)$ at T $\geqslant$ 948 K. This structural sequence is the same as that reported previously for $Sr_{0.8}Ce_{0.2}MnO_3$,[28] although the transition temperature is higher in $Sr_{0.7}Ce_{0.3}MnO_3$. The Sr and Ce cations are disordered on the perovskite $A$-site. Structure refinements were carried out for all temperature runs using the protocol described in the previous section. Figure 1 shows the neutron diffraction pattern recorded at 4.2 K and fitted using the tetragonal structure in $I4/mcm$ (the crystallographic parameters are listed in Table I). It is worthwhile to note that the oxygen displacement parameters are rather large at 4.2 K ($\sim$0.02 Å$^2$, compared to $\sim$0.003 Å$^2$ found in $LaMnO_3$[29] at 20 K), and they do not change much with increasing temperature (up to 373 K, the highest temperature in the cryostat), indicating the suppression of the coherent static Jahn-Teller distortion in $Sr_{0.7}Ce_{0.3}MnO_3$.[10]

As shown in Fig. 1, there is no evidence for a magnetically ordered structure at 4.2 K, in contrast to $Sr_{0.65}Pr_{0.35}MnO_3$,[30] which transforms to a C-type antiferromagnetic (C-AFM) structure at 250 K. It is interesting to compare $Sr_{0.7}Ce_{0.3}MnO_3$ with $Sr_{0.65}Pr_{0.35}MnO_3$ as the lanthanoid content is similar in these two compounds. One obvious difference between them is the valence of the lanthanoid. Ce ions are multivalent (30% $Ce^{3+}$/70% $Ce^{4+}$) in $Sr_{0.7}Ce_{0.3}MnO_3$,[10] whereas Pr ions are 3+ in $Sr_{0.65}Pr_{0.35}MnO_3$. While the ionic radius of $Ce^{3+}$ (1.143 Å) is very similar to that of $Pr^{3+}$ (1.126 Å), $Ce^{4+}$ ions (0.97 Å) are much smaller (especially compared with $Sr^{2+}$ [1.26 Å]).[31] Note that the ionic radii quoted here are for eightfold coordinated cations—the highest coordination number for which tabulated data are available for all cations. The presence of mixed $Ce^{3+}$ and $Ce^{4+}$ introduces extra disorder in $Sr_{0.7}Ce_{0.3}MnO_3$. This disorder can be quantified by the variance $\sigma^2$ of the $A$-site radius distribution ($\sigma^2 = \sum y_i {r_i}^2 - \langle r_A\rangle^2$, where $r_i$ is the ionic radius of the $A$-site cations, $y_i$ the corresponding fractional occupancy, and $\langle r_A\rangle$ is the average $A$-site cation radius).[32,33] It has been demonstrated previously that both $\langle r_A\rangle$ and $\sigma^2$ are key chemical variables that control important physical properties in hole-doped manganites.[32–36] Although the average $A$-site cation radius $\langle r_A\rangle$ is similar (1.189 Å for $Sr_{0.7}Ce_{0.3}MnO_3$ and 1.213 Å for $Sr_{0.65}Pr_{0.35}MnO_3$), the variance ($\sigma^2$) of the $A$-site radius distribution is much larger for $Sr_{0.7}Ce_{0.3}MnO_3$ (0.014 Å$^2$) than that for $Sr_{0.65}Pr_{0.35}MnO_3$ (0.004 Å$^2$). This might explain why these two seemingly similar compounds behave so differently. The increased $A$-site disorder in $Sr_{0.7}Ce_{0.3}MnO_3$ has been suggested previously to be responsible for the suppression of the cooperative Jahn-Teller effect,[10] which, in turn, might destroy the long-range antiferromagnetic order observed in samples with lower Ce concentrations.[8,13,14]

Temperature dependencies of the appropriately scaled lattice parameters and the equivalent primitive cell volume are shown in Figs. 2(a) and 2(b), respectively, which suggest that the thermally induced $I4/mcm$ $(a^0a^0c^-) \leftrightarrow Pm\bar{3}m$ $(a^0a^0a^0)$ phase transition is continuous. Based on group theoretical analysis by Carpenter and Howard,[37] this transition can be driven by the tilting of $MnO_6$ octahedra alone, or a combination of octahedral tilting and cooperative Jahn-Teller distortions. The irreducible representations (irreps) associated with these two structural instabilities are identified as $R_4^+$ and $\Gamma_3^+$ of the space group $Pm\bar{3}m$, respectively.[37] This $I4/mcm \leftrightarrow Pm\bar{3}m$ transition can be described using a Landau free-energy expansion that includes order parameters associated with the irreps $R_4^+$ and $\Gamma_3^+$. The nature of the continuous phase transition can be established by examining the temperature dependence of the order parameter ($Q$), e.g., $Q \sim (T_c - T)^n$, with $n = 1/2$ or $1/4$ for a second-order or tricritical transition, as solutions to standard Landau 2-4 ($G[Q] = 1/2A[T - T_c]Q^2 + 1/4BQ^4$) and 2-6 ($G[Q] = 1/2A[T - T_c]Q^2$

TABLE I. Crystallographic parameters for $Sr_{0.7}Ce_{0.3}MnO_3$ at 4.2 K. The number in parentheses beside each entry indicates the estimated standard deviation referred to the last digit shown. For O1, $U^{12} = U^{13} = U^{23} = 0$. For O2, $U^{13} = U^{23} = 0$. $U_{equ} = (U^{11} + U^{22} + U^{33})/3$. Space group: $I4/mcm$, $a = b = 5.4340(1)$ Å, $c = 7.7299(4)$ Å, $R_{wp} = 7.60\%$, $R_p = 6.46\%$, $\chi^2 = 2.78$.

| Atom | Site | $x$ | $y$ | $z$ | $U^{11} = U^{22}$ ($10^{-2}$ Å$^2$) | $U^{33}$ ($10^{-2}$ Å$^2$) | $U^{12}$ ($10^{-2}$ Å$^2$) | $U_{iso}$ / $U_{equ}$ ($10^{-2}$ Å$^2$) |
|---|---|---|---|---|---|---|---|---|
| Sr/Ce | 4$b$ | 0 | 0.5 | 0.25 | | | | 0.863(33) |
| Mn | 4$c$ | 0 | 0 | 0 | | | | 0.58(5) |
| O1 | 4$a$ | 0 | 0 | 0.25 | 4.07(13) | 0.19(11) | 0 | 2.77(12) |
| O2 | 8$h$ | 0.2209(2) | $= x + 0.5$ | 0 | 0.83(4) | 4.31(11) | 0.54(6) | 1.99(7) |

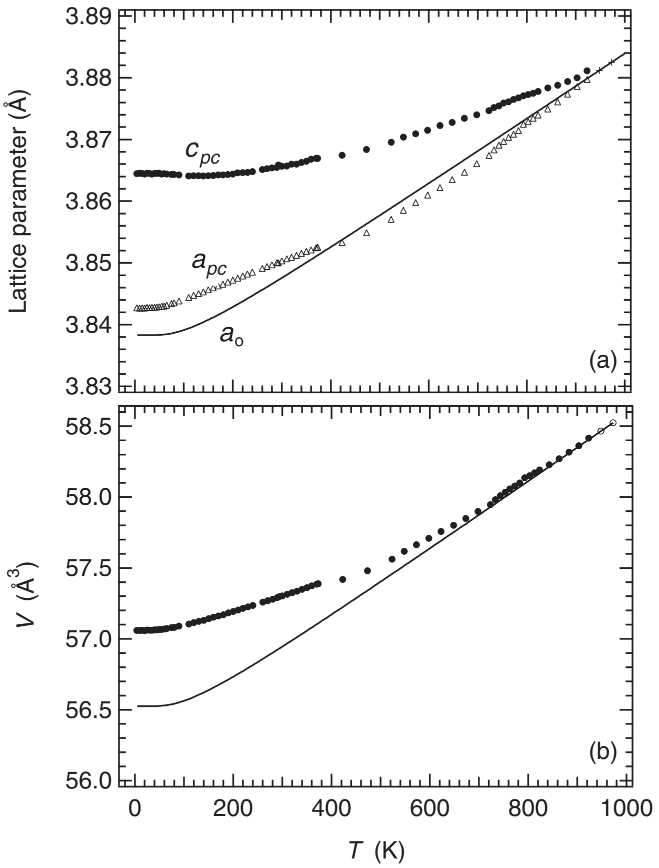

FIG. 2. Temperature dependence of (a) the appropriately scaled lattice parameters $a_{pc}$ $( = a/\sqrt{2})$ and $c_{pc}$ $( = c/2)$, and (b) the equivalent primitive cell volume for $Sr_{0.7}Ce_{0.3}MnO_3$. The solid line in (b) is a fit to the data in the cubic phase using the equation $V_o = V_1 + V_2\Theta_{s1}\coth\frac{\Theta_{s1}}{T}$ with $\Theta_{s1}$ fixed at 150 K (see text for details). The solid line in (a) is the reference parameter $a_o$, obtained from $a_o = V_o{}^{1/3}$. Note that experimental uncertainties are smaller than the size of the symbols used.

$+ 1/6CQ^6$) potentials, respectively.[20] For octahedral tilting transitions in perovskites, the order parameter is represented by the tilt angle ($\phi$ ), which can be estimated from the oxygen coordinate, $\phi = \tan^{-1}(1 - 4x[O2])$.[38] As shown in Fig. 3, $\phi^4$ varies linearly with temperature for $Sr_{0.7}Ce_{0.3}MnO_3$ (except near T = 0 K due to saturation effects[39,40]), with an extrapolation to zero at $T_{c,\phi} = 938 \pm 5$ K. The $\phi^4$ temperature dependence is the same as that observed recently in our study of $Sr_{0.8}Ce_{0.2}MnO_3$,[28] and in both cases, it is clear that the tetragonal to cubic transition is close to tricritical in nature. This behavior is different from that seen in $Sr_{0.65}Pr_{0.35}MnO_3$,[30] where a linear relationship between $\phi^2$ and temperature indicates a second-order tetragonal to cubic transition. The value of the fourth-order coefficient of the Landau expansion for these materials clearly varies (near zero for tricritical; positive for second order), as is not uncommon for tilting transitions in perovskites. For example, the cubic ↔ tetragonal transition in $SrZrO_3$ is tricritical,[41] while the same transition in $SrHfO_3$ appears to be second order.[42] However, it is unclear why subtle changes in chemistry and/or disorder should lead to a change in the nature of phase transitions, and this is the subject of ongoing experimental studies.

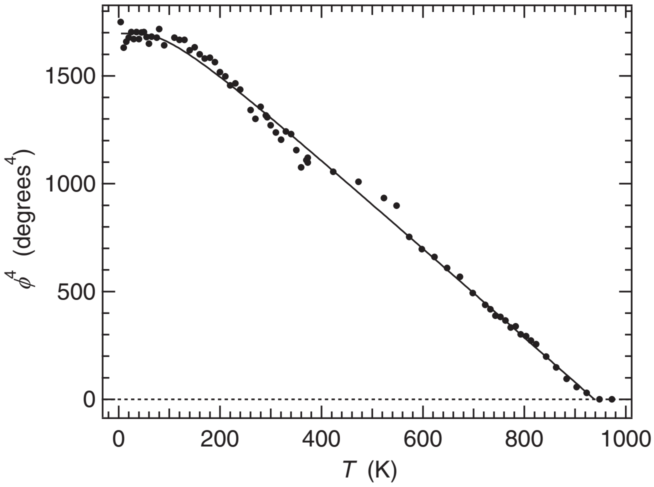

FIG. 3. Temperature dependence of the fourth power of the octahedral tilt angle for $Sr_{0.7}Ce_{0.3}MnO_3$. The solid line is a fit to the data using the Landau solution $\phi^4 = A\frac{\Theta_{s2}}{T_{c,\phi}}[\coth(\frac{\Theta_{s2}}{T_{c,\phi}}) - \coth(\frac{\Theta_{s2}}{T})]$,[15] with $A = 1957.6^{\circ 4}$, $\Theta_{s2} = 131.5$ K, and $T_{c,\phi} = 938.1$ K.

The spontaneous strains can be derived from the refined lattice parameters. The linear strain components $e_1$, $e_2$, and $e_3$ are given by

$$e_1 = e_2 = \frac{a_{pc} - a_o}{a_o} = \frac{\left(\frac{a}{\sqrt{2}} - a_o\right)}{a_o},$$

$$e_3 = \frac{c_{pc} - a_o}{a_o} = \frac{\left(\frac{c}{2} - a_o\right)}{a_o}$$

for the $I4/mcm$ structure.[17–19] The reference parameter, $a_o$ $( = V_o{}^{1/3})$, is the lattice parameter of the cubic structure extrapolated to lower temperatures. The temperature dependence of $V_o$ must be such that it has a zero slope as T approaches 0 K due to saturation effects.[39,40] This can be effectively described by a function of the form[43]

$$V_o = V_1 + V_2\Theta_{s1}\coth\frac{\Theta_{s1}}{T},$$

where $\Theta_{s1}$ is the saturation temperature for the thermal expansion of the cubic structure. Since there are only two data points available in the cubic phase region, it is not possible to obtain a fit for the above equation with $\Theta_{s1}$ as a free parameter. Based on the known values of saturation temperature for $SrTiO_3$ (~140 K),[44] $LaAlO_3$ (~250 K),[43] and $(La,Pr)AlO_3$ (~300 K),[16] $\Theta_{s1}$ for $Sr_{0.7}Ce_{0.3}MnO_3$ was fixed (somewhat arbitrarily) at 150 K in the current study. The fit for $V_o$ in Fig. 2(b) was then obtained by matching the cell volume ($V_o$) with that measured at 973 and 948 K. The symmetry-adapted strains,[21] $e_t$ and $e_a$, are a combination of the linear strain components, $e_1$, $e_2$, $e_3$, as

$$e_t = \frac{1}{\sqrt{3}}(2e_3 - e_1 - e_2) = \frac{c - \sqrt{2}a}{\sqrt{3}a_o},$$

$$e_a = e_1 + e_2 + e_3 = \frac{(\sqrt{2}a + c/2 - 3a_o)}{a_o}.$$

Figure 4 shows the temperature dependence of the tetragonal strain ($e_t$) and the volume strain ($e_a$); the irregular pattern of evolution suggests that both strains include contributions from

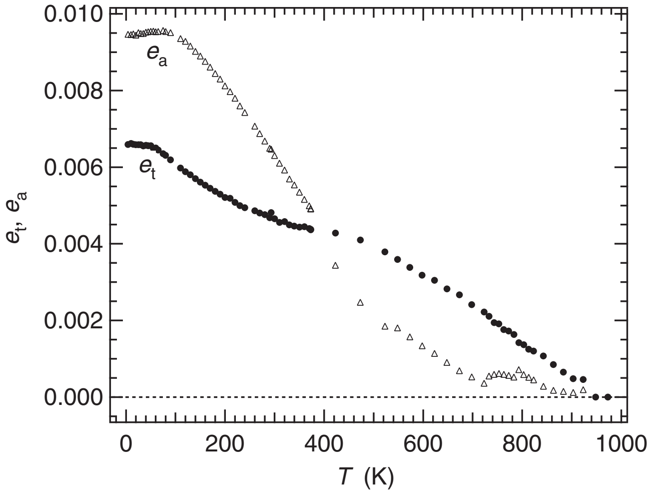

FIG. 4. Temperature dependence of the symmetry-adapted strains, $e_t$ and $e_a$. The irregularity of this unusual pattern of evolution shows clearly that there is more than one process contributing to the overall structural changes.

more than one structural mechanism. Although the volume strain $e_a$ is sensitive to the choice of $a_o$, which is not very accurate in the current study (due to limited data points in the cubic phase), the derived $e_a$ is similar to that found for $LaMnO_3$ (~0.008)[45] as a result of the Jahn-Teller distortion of the $MnO_6$ octahedra.

The following discussion focuses on the tetragonal strain $e_t$, since its values are insensitive to the choice of $a_o$, and, therefore, are more reliable. Readers unfamiliar with this approach are referred to previous publications by Carpenter *et al.*,[16] Carpenter,[44] and Carpenter and Howard[45] for other worked examples. The tetragonal strain is expected to vary with $\phi^2$ for the $I4/mcm \leftrightarrow Pm\bar{3}m$ octahedral tilting transition (if no other structural instability is involved).[21] However, $e_t$ shows an irregular dependence on $\phi^2$ (Fig. 5), and the expected linear relationship between $e_t$ and $\phi^2$ is only maintained from $T_{c,\phi}$ down to ~800 K (which confirms that the $I4/mcm \leftrightarrow Pm\bar{3}m$ transition is induced by the octahedral tilting alone). This provides a clear indication of the onset of an additional structural change around 800 K. Additional evidence comes from the temperature dependence of the Mn-O bond lengths. Figure 6 reveals a noticeable change in the thermal expansion of the Mn-O(2) bond length around 800 K, with the length remaining approximately constant above ~800 K. The pattern of evolution is interpreted in terms of a tilting transition at $T_{c,\phi}$ ~ 938 K ($Pm\bar{3}m \leftrightarrow I4/mcm$, $R_4^+$) followed by an isosymmetric transition attributed to electronic Jahn-Teller–like behavior at $T_{c,\mathrm{JT}}$ ~ 800 K ($I4/mcm$, $R_4^+ \leftrightarrow I4/mcm$, $R_4^+$ and $\Gamma_3^+$).

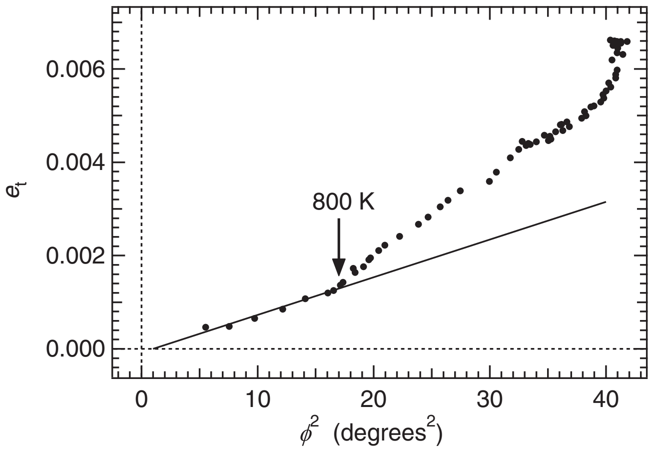

FIG. 5. The tetragonal strain, $e_t$, as a function of the square of the tilt angle ($\phi^2$), showing an irregular dependence with a marked break in slope (corresponding to T ~ 800 K). The straight line is a fit to data obtained at 803 ⩽ T ⩽ 923 K; it is within experimental uncertainty of passing through the origin.

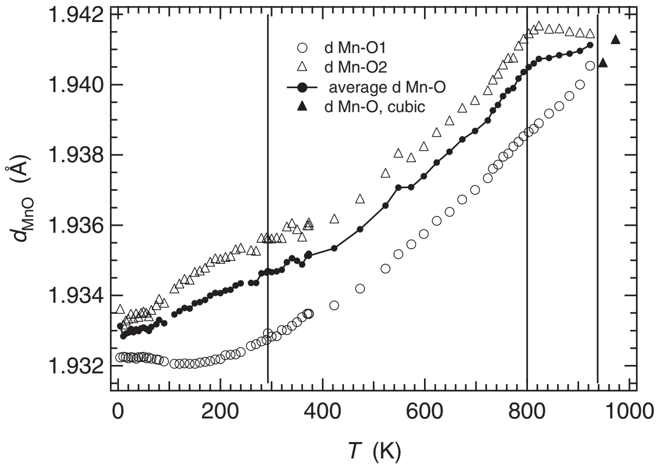

FIG. 6. Mn-O bond lengths as a function of temperature. The open circles, open triangles, and solid triangles represent the Mn-O distance for apical oxygens ($d_{\mathrm{Mn-O1}}$), the Mn-O distance for equatorial oxygens ($d_{\mathrm{Mn-O2}}$), and the bond distance in the cubic phase, respectively. The average Mn-O bond length in the tetragonal phase is also plotted (solid circles connected by straight lines). Vertical lines shown at 938, 800, and 293 K correspond, respectively, to the octahedral tilting transition temperature, the approximate position for the onset of additional octahedral distortions, and a peak in the heat capacity (see following section).

An unusual feature evident in Fig. 6 is the nature of the $MnO_6$ octahedral distortion. The most commonly encountered manifestation of the Jahn-Teller effect for perovskites $ABO_3$ with $I4/mcm$ symmetry is a tetragonal elongation of the $BO_6$ octahedra such that the two axial Mn-O(1) distances are longer than the four equatorial Mn-O(2) distances. This is seen in related oxides such as $Sr_{0.8}Ce_{0.2}MnO_3$[28] and $Sr_{0.65}Pr_{0.35}MnO_3$,[30] as well as $SrMn_{0.5}Ru_{0.5}O_3$[46,47] and $SrMn_{0.5}Sb_{0.5}O_3$.[47] In the present case, the four equatorial Mn-O(2) bonds are slightly longer than the two axial Mn-O(1) bonds. The transition from axially elongated to axially compressed octahedra in the series $Sr_{1-x}Ce_xMnO_3$ was first noted by Sundaresan *et al.*[8] at $0.3 < x < 0.4$, although in that work and in our subsequent study,[7] it was assumed that the transition from elongated to compressed octahedra was a consequence of the redistribution of Mn $3d$ electrons, with the electron switching from the $d_z{}^2$ orbital to the $d_x{}^2\text{-}_y{}^2$ orbital as the structure evolved from tetragonal to orthorhombic. The observation that the $MnO_6$ octahedra become compressed in the tetragonally structured $Sr_{0.7}Ce_{0.3}MnO_3$ suggests that the situation is more complex.

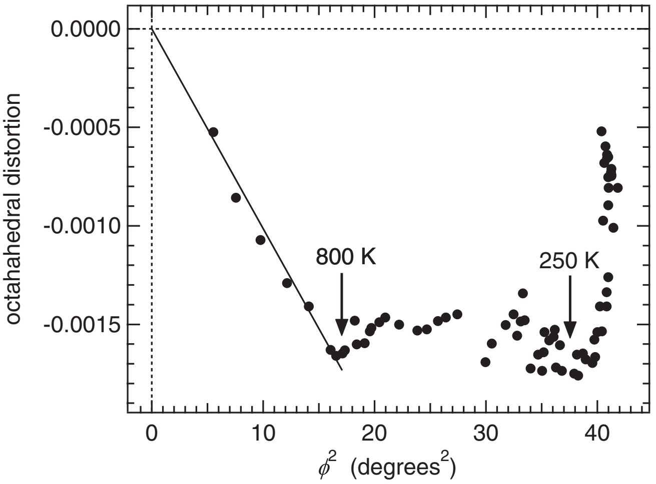

FIG. 7. The octahedral distortion as a function of the square of the tilt angle ($\phi^2$), showing a linear relationship between $T_{c,\phi}$ and ~800 K. A straight-line fit in this temperature range gives the amount of distortion expected for a given tilt angle ($-0.0001014\phi^2$). At T < 250 K, the octahedral distortion decreases further.

In tetragonally structured $ABO_3$ perovskites, the $BO_6$ octahedra are tilted relative to each other as a result of the conflicting bonding requirements of the $A$- and $B$-type cations. These tilts introduce distortions of the $BO_6$ octahedra, although such distortions are typically small, as evident in $SrTiO_3$,[48] $SrZrO_3$[41] (both in space group $I4/mcm$, tilt system $a^0a^0c^-$), and $NaTaO_3$[49] (in $P4/mbm$, $a^0a^0c^+$). Although it was speculated by Darlington[50] that the octahedra in tetragonal $I4/mcm$ and $P4/mbm$ perovskites will be invariably elongated along the octahedral rotation axis, there are many examples of compressed octahedra as a result of tilting (in the absence of a Jahn-Teller distortion), e.g., $SrZrO_3$,[41] $NaTaO_3$,[49] $CaTiO_3$,[51] $SrRuO_3$,[52] and $SrHfO_3$.[42] In the present case of $Sr_{0.7}Ce_{0.3}MnO_3$, the tetragonally compressed octahedra might be brought about by a combination of octahedral tilting and Jahn-Teller–like distortion, with the former causing octahedral compression and the latter elongation, resulting in a net effect of small compression.

The octahedra retain a tetragonal geometry within $I4/mcm$ symmetry, and their distortion can be represented using the bond lengths in a manner that is analogous to the definition of the tetragonal strain:

$$\text{Octahedral distortion} = \frac{1}{\sqrt{3}}\left(\frac{2d_{\text{Mn-O1}} - 2d_{\text{Mn-O2}}}{(1/3)(d_{\text{Mn-O1}} + 2d_{\text{Mn-O2}})}\right).$$

Figure 7 shows the octahedral distortion plotted against the square of the tilt angle ($\phi^2$). Since the $MnO_6$ octahedra are axially compressed, the overall octahedral distortion is negative. For a simple tilting transition, the graph is expected to be a straight line passing through the origin. Therefore, the linear fit shown in the temperature range of 803–923 K (octahedral distortion $= -0.0001014\phi^2$) gives a quantitative relationship for the amount of distortion due to tilting alone, and it has been used to estimate the octahedral tilting contribution at all temperatures (Fig. 8). Evidently, the tetragonal compression of the octahedra at T < 803 K is less than that predicted from the tilting alone. This difference might be attributed to the "Jahn-Teller" effect, which has then been determined by subtracting the tilting contribution from the total octahedral distortion (Fig. 8). Figure 9 shows the temperature dependence of the square of the excess octahedral distortion, which varies approximately linearly with temperature between ~250 and 800 K. The solid line is a fit to data between 293 and 783 K using an expression with the same form as that used to describe the tilting in Fig. 3:

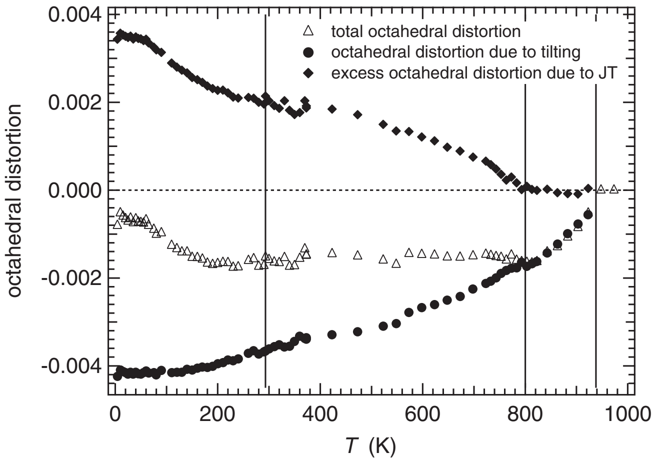

FIG. 8. Excess octahedral distortion (including the "Jahn-Teller" component), calculated as the difference between the observed distortion and the contribution from octahedral tilting, as a function of temperature. Vertical lines are at the same temperatures as shown in Fig. 6.

$$(\text{Octahedral distortion})^2 = A\frac{\Theta_{s3}}{T_{c,\text{JT}}}\left[\coth\left(\frac{\Theta_{s3}}{T_{c,\text{JT}}}\right) - \coth\left(\frac{\Theta_{s3}}{T}\right)\right],$$

where $\Theta_{s3}$ is a saturation temperature. This accounts for the leveling off of the order parameter as $T \to 0$ K, and it has been used successfully to describe the evolution of the Jahn-Teller order parameter in $(La,Pr)AlO_3$.[16,53] If we believe that the

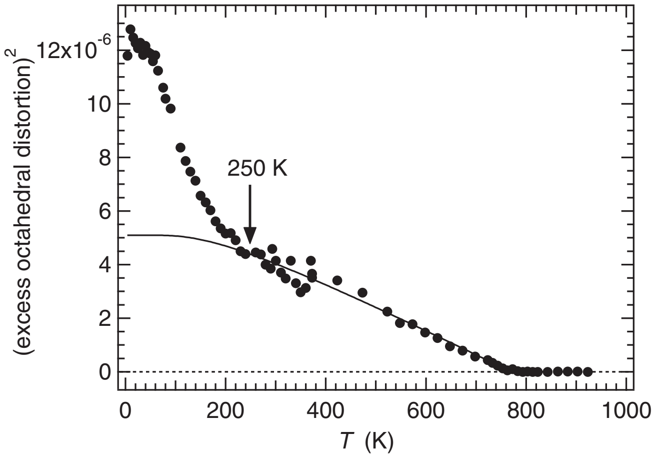

FIG. 9. The square of the excess octahedral distortion as a function of temperature. The solid curve is a fit to the data between 293 and 783 K using the equation (Octahedral distortion)$^2$ = $A\frac{\Theta_{s3}}{T_{c,\text{JT}}}[\coth(\frac{\Theta_{s3}}{T_{c,\text{JT}}}) - \coth(\frac{\Theta_{s3}}{T})]$, giving $A = 7.233 \times 10^{-6}$, $T_{c,\text{JT}} = 770$ K, and $\Theta_{s3} = 256$ K.

excess octahedral distortion is related to the influence of a "Jahn-Teller" order parameter, $Q_{\mathrm{JT}}$, which varies linearly with the distortion, the data would imply a second-order transition at $T_{c,\mathrm{JT}} = 770 \pm 13$ K (Fig. 9).

A second notable feature of the octahedral distortion is that its absolute value decreases at temperatures below ~250 K (Fig. 7). We have already shown that the overall octahedral compression is reduced at T < 800 K (Fig. 8), from that expected from tilting alone, by a Jahn-Teller–like distortion that evidently favors elongation of the $\mathrm{MnO_6}$ octahedra. Apparently, there is a second contribution toward the reduction in the octahedral compression at T < 250 K (Fig. 9). These distortions appear to occur independently of the evolution of the octahedral tilt angle with temperature, which does not show major anomalies near 800 or 250 K (Fig. 3). The implication is that coupling between the tilting and electronic/magnetic effects is weak.

In summary, the strain data are consistent with four separate contributions to the structural evolution of $\mathrm{Sr_{0.7}Ce_{0.3}MnO_3}$ in the temperature range of 4.2–973 K. First, there is normal thermal expansion of the cubic structure. Second, a phase transition at 938 ± 5 K is driven by octahedral tilting to give the tetragonal structure in $I4/mcm$. Evolution of the octahedral tilt angle with temperature is consistent with this transition being tricritical in character (${Q_{\mathrm{tilt}}}^4$ proportional to T, Fig. 3). Tilting induces a negative distortion (compression) of the $\mathrm{MnO_6}$ octahedra (the axial bond length $d_{\mathrm{Mn-O1}}$ shorter than the equatorial one $d_{\mathrm{Mn-O2}}$). There then appears to be a discrete, isosymmetric Jahn-Teller—like transition at 770 ± 13 K, which superimposes on the $\mathrm{MnO_6}$ octahedra a strain in the opposite sense. This gives rise to a positive volume strain, as is observed also for the Jahn-Teller transition in $\mathrm{LaMnO_3}$.[45] The octahedral distortion is used as a Jahn-Teller order parameter, $Q_{\mathrm{JT}}$; the transition is isosymmetric and therefore might be expected to be first order in character,[54] but, in this case, it appears to be second order (${Q_{\mathrm{JT}}}^2$ proportional to T, Fig. 9), as appears to be the case in $\mathrm{La_{0.9}Ba_{0.1}MnO_3}$.[45] Finally, there is a further increase in the excess octahedral distortion at temperatures below 250 K (Fig. 9).

The most obvious explanation of the unusual pattern of strain (Fig. 4) and bond length (Fig. 6) variations is that there are indeed two separate structural instabilities, the first being due to octahedral tilting and the second due to cooperative distortions relating to the electronic structure. However, this requires that the sense of octahedral distortion favored by each is opposite—compressed octahedra favored by tilting and elongated octahedra favored by "Jahn-Teller" distortions. The observed bond lengths are only averages, which could hide the true dimensions of individual octahedra through the effects of both static and dynamic disordering, as demonstrated in the case of $\mathrm{LaMnO_3}$.[55,56] Some local probe of the bond length variations might help to confirm or refute this interpretation. The additional change in the trend of octahedral distortion below ~250 K is too far from the temperature of the heat-capacity anomaly at 293 K (see following section) for the two effects to be strongly correlated. However, the heat-capacity anomaly is quite extensive (roughly between 275 and 300 K, as will be seen in Fig. 11 below), so it is conceivable that this anomaly might be associated with the marked break in the slope of the square of the excess octahedral distortion (~250 K, Fig. 9), especially considering the complicated coupling among the lattice, orbital, and spin degrees of freedom in this system.

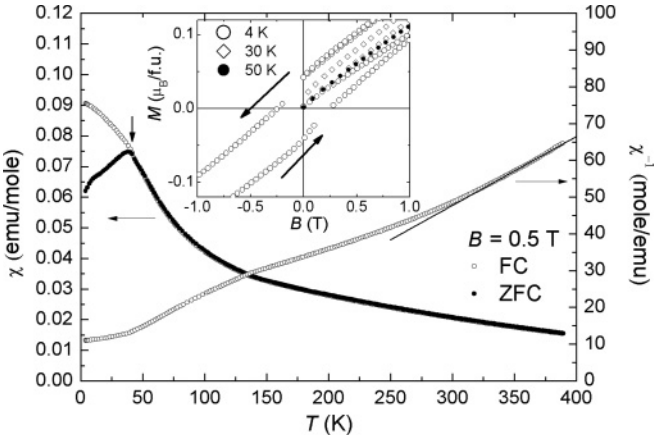

FIG. 10. Temperature dependence of the magnetic susceptibility ($\chi$) and its reciprocal ($\chi^{-1}$) collected in the field-cooling (FC) and zero-field-cooling (ZFC) conditions. The solid line is a fit of the data using the Curie-Weiss (CW) law over the temperature range 390–300 K. The inset shows the hysteresis loop opening below ~40 K in the $M(B)$ dependence.

### B. Physical properties

The temperature dependence of the field-cooled (FC) and zero-field-cooled (ZFC) DC magnetic susceptibility $\chi$ is shown in Fig. 10 together with its reciprocal; our results are in good agreement with those obtained by Sundaresan *et al.*[8] In the temperature range of 390–300 K, $\chi_{\mathrm{FC}}$(T) may be analyzed using the Curie-Weiss (CW) law: $\chi(T) = \mathrm{C}/(\mathrm{T} - \theta_{\mathrm{CW}})$, where the Curie constant $\mathrm{C} = \mathrm{N}{\mu_{\mathrm{eff}}}^2/3\mathrm{k_B}$, $\mu_{\mathrm{eff}}$ stands for the effective moment, and $\theta_{CW}$ is the characteristic Curie-Weiss temperature. A least-square fit yields values of $\mu_{\mathrm{eff}} = 6.5\mu_{\mathrm{B}}$/f.u. and $\theta_{\mathrm{CW}} = 45.2$ K. Positive $\theta_{\mathrm{CW}}$ is characteristic of ferromagnetic correlation between spins ($\theta_{\mathrm{CW}}$ is proportional to the effective exchange parameter

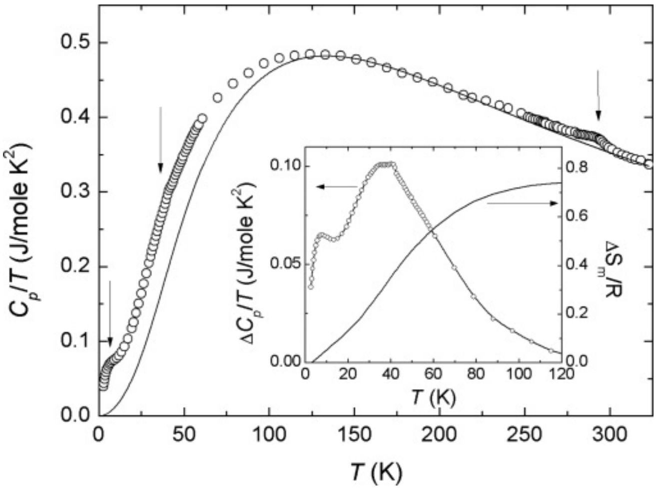

FIG. 11. The $C_{\mathrm{p}}/T$ ratio as a function of temperature. The solid line is a lattice contribution derived from the Debye approximation. Depicted in the inset are the magnetic contribution $\Delta C_{\mathrm{p}}/T$ and magnetic entropy $\Delta S_{\mathrm{m}}$ at temperatures below 120 K.

between magnetic spins). Based on XANES results,[10] there are 0.09 f.u. $\mathrm{Ce}^{3+}$, 0.21 f.u. $\mathrm{Ce}^{4+}$, 0.52 f.u. $\mathrm{Mn}^{3+}$, and 0.48 f.u. $\mathrm{Mn}^{4+}$ in $\mathrm{Sr}_{0.7}\mathrm{Ce}_{0.3}\mathrm{MnO}_3$. The effective moment derived from the Curie-Weiss law is larger than that predicted from the combination of effective moments associated with $\mathrm{Ce}^{3+}$ ($\mu_{\mathrm{eff}} = 2.54\mu_{\mathrm{B}}$), $\mathrm{Mn}^{3+}$ ($\mu_{\mathrm{eff}} = 3.87\mu_{\mathrm{B}}$), and $\mathrm{Mn}^{4+}$ ($\mu_{\mathrm{eff}} = 4.9\mu_{\mathrm{B}}$), giving rise to $\mu_{\mathrm{eff}} = (0.09\mu_{\mathrm{eff}}{}^2[\mathrm{Ce}^{3+}] + 0.52\mu_{\mathrm{eff}}{}^2[\mathrm{Mn}^{3+}] + 0.48\mu_{\mathrm{eff}}{}^2[\mathrm{Mn}^{4+}])^{1/2} = 4.6\mu_{\mathrm{B}}/\mathrm{f.u.}$ Note that it is generally accepted to use spin-only values of the effective moment for $3d$ ions, where the orbital contribution is totally quenched. The values of $\mu_{\mathrm{eff}}$ and $\theta_{\mathrm{CW}}$ are only valid over the temperature range 390–300 K, as the overall shape of $\chi^{-1}(T)$ dependence is not linear. Such a nonlinear relationship between $\chi^{-1}(T)$ and temperature was also found in other manganites in the paramagnetic state, which was associated with superparamagnetic behavior[57] or polaronic state[58,59]—both scenarios are consistent with a higher effective moment than that predicted for independent, paramagnetic spins. The presence of magnetic clusters was already proposed by Mandal *et al.*[11] for $\mathrm{Sr}_{1-x}\mathrm{Ce}_x\mathrm{MnO}_3$ ($x = 0.25, 0.35$) at high temperatures (up to 450–500 K). Also shown in Fig. 10 is the split between $\chi_{\mathrm{FC}}$ and $\chi_{\mathrm{ZFC}}$ at temperatures below 41 K. The FC branch saturates as T approaches 0 K, whereas the ZFC component forms a cusp at ∼38 K and then decreases. Since no long-range magnetic ordering was observed with neutron scattering at low temperatures (see previous section), the observed FC-ZFC branching is attributed to the presence of spin-glass, where the presence of irreversibility is related to the freezing/melting of magnetic spins or clusters. A temperature where irreversibility of magnetic susceptibility occurs is called a freezing temperature $T_f$,[60] which is found to be around 41 K for $\mathrm{Sr}_{0.7}\mathrm{Ce}_{0.3}\mathrm{MnO}_3$ in a magnetic field of 0.5 T. This is in good agreement with previous reports.[8,11]

We also investigated a field dependence of the magnetization, collected at various temperatures. At temperatures above $T_f$, the magnetization curves ($M$) show a relationship close to linear with the applied magnetic field ($B$) without any trace of a hysteresis loop (not shown). In the spin-glass regime (T < 40 K), hysteresis loops are observed (inset of Fig. 10). At 4 K, the hysteresis loop is very extended and narrow with a coercive field $B_{\mathrm{c}}$ of about 0.25 T, indicating that $\mathrm{Sr}_{0.7}\mathrm{Ce}_{0.3}\mathrm{MnO}_3$ is a soft magnetic material, which, together with the very weak remnant field $M_{\mathrm{r}}$ (0.042 $\mu_{\mathrm{B}}$/f.u. at 4 K), is typical for materials with short-range magnetic ordering.

A temperature dependence of the heat capacity over temperature ($C_{\mathrm{p}}/T$ ratio) is displayed in Fig. 11, clearly showing three distinct anomalies at about 293 K, 41 K, and 7 K. The high-temperature anomaly seems to be quite extensive (roughly between 275 and 300 K), and its presence might be related to the marked break in the slope of the square of the excess octahedral distortion (∼250 K, Fig. 9). As the anomaly at 41 K coincides with the freezing temperature $T_f$, it can be associated with the formation of the spin-glass state. The nature of the anomaly around 7 K, well within the spin-glass regime, is unclear.

One can roughly estimate the magnetic contribution to the heat capacity, assuming that at temperatures between 130 K and 250 K (below 130 K, the magnetic susceptibility increases rapidly due to the short-range magnetic correlations, being precursors of the spin-glass state) the impact of magnetic effects is negligible compared to the lattice contribution to the total heat capacity and the investigated material is semiconducting (i.e., no contribution from band electrons).[8,61] In order to do that, we have separated the total $C_{\mathrm{p}}$ collected in this temperature range into a sum of two Debye terms, $C_{\mathrm{L}} = 2C_D(\Theta_{\mathrm{D1}}) + 3C_D(\Theta_{\mathrm{D2}})$, resulting from phononic contributions of the cation and anion sublattices, respectively. The lattice heat capacity, $C_D$, is given by the following formula according to the Debye model:

$$C_D = 9R\left(\frac{T}{\theta_D}\right)^3 \int_0^{\frac{\theta_D}{T}} \frac{x^4 e^x}{(1-e^x)^2}dx,$$

where $R$ stands for the gas constant, and $\theta_{\mathrm{D}}$ is the characteristic Debye temperature. The best fit to the data is shown in Fig. 11 as a solid line, and the characteristic Debye temperatures were obtained from the fit: $\theta_{\mathrm{D1}} = 328(8)$ K (cations) and $\theta_{\mathrm{D2}} = 679(6)$ K (oxygen). The magnetic contribution to the heat capacity can then be simply derived by subtracting the lattice contribution from the observed heat capacity: $\Delta C_{\mathrm{p}}/T = C_{\mathrm{p}}/T - C_{\mathrm{L}}/T$ (inset of Fig. 11). As seen, the low-temperature anomalies are better defined in the form of extended bumps at about 7 and 40 K. Magnetic entropy calculated from $T_0 = 2.6$ K, given by $\Delta S_m(T) = \int_{T_0}^{T}\frac{\Delta C_p}{T}dT$, reaches the value of only $0.35R$ (∼2.9 J/mol K) at 40 K, i.e., much lower than the value of $S_m = 0.52R\ln 4 + 0.48R\ln 5 = 12.4$ J/mol K (as predicted for a long-range magnetic ordering transition, which supports the formation of spin-glass). The amount of entropy associated with the high-temperature anomaly (∼293 K) is estimated as only $0.02R$ (∼0.16 J/mol K). It should be mentioned that these estimations are based on a simple model, ignoring other possible, but weaker, effects at lower temperatures. The emphasis of the analysis is to show that the magnetic contribution is much smaller than that expected in systems with long-range magnetic ordering.

In summary, we have observed three different anomalies at about 293, 41, and 7 K by analyzing the temperature dependence of the magnetic susceptibility and heat capacity. The presence of the anomaly around room temperature in the $C_{\mathrm{p}}/T$ data appears to be quite extensive in temperature; it occurs at ∼40 K above a further increase in the excess octahedral distortion (Fig. 9) evident from the structural studies. The exact origin of this is unknown; however, it is known in $\mathrm{Sr}_{0.65}\mathrm{Pr}_{0.35}\mathrm{MnO}_3$[30] that the long-range magnetic order impacts on the magnitude of the octahedral distortion. As magnetic susceptibility shares some features with polaronic systems, it seems reasonable to postulate that the additional lattice distortion may be related to some kind of magnetoelastic coupling between local magnetic moments and lattice degrees of freedom. It appears that in strongly frustrated materials, due to the magnetoelastic coupling, the atomic motion helps to release the magnetic frustration by supporting more energetically preferred local magnetic configurations. Such a coupling among magnetic, charge, and lattice degrees of freedom has been observed in hexagonal $R\mathrm{MnO}_3$ antiferromagnets (where $R$ = Ho, Yb, Sc, Y).[62] The other possibility is the presence of local charge-ordered regions that melt around room temperature.[63,64] Indeed, a charge-ordered state was suggested to occur in $\mathrm{Sr}_{1-x}\mathrm{Ce}_x\mathrm{MnO}_3$ ($0.15 \leqslant x \leqslant 0.35$) by Mandal and coworkers,[11] based on their magnetic and electrical transport measurements. However, if this phenomenon occurs in our sample, the coherent length must be less than what could be observed by neutron diffraction. Magnetic frustration, caused by the competition between the ferromagnetic (via Mn$^{3+}$-O$^{2-}$-Mn$^{4+}$ double-exchange) and antiferromagnetic (via Mn$^{3+}$-O$^{2-}$-Mn$^{3+}$, Mn$^{4+}$-O$^{2-}$-Mn$^{4+}$ super-exchange) interactions,[65] gives rise to the formation of spin-glass state at $T_f = 41$ K. The difference between FC and ZFC magnetic susceptibility at temperatures below $T_f$, the narrow and extended hysteresis loops observed in the magnetization measurements, and the very low magnetic entropy released at $T_f$, together with the absence of any magnetic peaks in the low-temperature neutron diffraction patterns, confirm the formation of a spin-glass state at low temperatures. A transition, from the antiferromagnetic ground state observed at low Ce concentrations[8,9,13,14] to the ground state with short-range magnetic order, is expected with increasing Ce content in Sr$_{1-x}$Ce$_x$MnO$_3$, as the effective number of Mn$^{3+}$-Mn$^{4+}$ pairs increases. The competition between different exchange mechanisms, giving rise to magnetic frustration, is strong enough to suppress long-range magnetic ordering. In such a case, the formation of a cluster-glass system, consisting of spatially confined magnetic clusters, is expected, which may be responsible for the magnetic behavior of our material at low temperatures. All significant criteria for a short-range magnetic ordering are met by Sr$_{0.7}$Ce$_{0.3}$MnO$_3$—structural, magnetic, and charge disorders and magnetic frustration related to the coexistence of ferro- and antiferromagnetic interactions.[60] These facts may explain the previously reported[11] sample dependence of the structural and physical properties, reflecting the fragile balance among various degrees of freedom (lattice, charge, orbital, and spin).

## IV. CONCLUSIONS

High-resolution neutron powder diffraction has been employed to determine the crystal structure of Sr$_{0.7}$Ce$_{0.3}$MnO$_3$ from 4.2 to 973 K. The resulting lattice parameter and structural data were used to derive symmetry-adapted spontaneous strains. An octahedral tilting transition $(Pm\bar{3}m \leftrightarrow I4/mcm,\ R_4^+)$ has been detected at $T_{c,\phi} \sim 938$ K, and an isosymmetric Jahn-Teller–like transition at $T_{c,\mathrm{JT}} \sim 770$ K $(I4/mcm,\ R_4^+ \leftrightarrow I4/mcm,\ R_4^+$ and $\Gamma_3^+)$ has been postulated to explain the unusual pattern of strain variations, with two instabilities ($R_4^+$ and $\Gamma_3^+$) causing the octahedra to distort in opposite senses. Based on the evolution of the order parameters with temperature, the tilting transition has nearly tricritical character, while the "Jahn-Teller" transition is close to second order. Strain analysis has also revealed an additional anomaly at temperatures below ~250 K, which might be associated with an anomaly observed in the heat-capacity measurements.

There is no long-range magnetic order in Sr$_{0.7}$Ce$_{0.3}$MnO$_3$, in contrast to Sr$_{1-x}$Ce$_x$MnO$_3$ samples with lower Ce contents where C-type antiferromagnetic ordering was reported.[8,13,14] It is proposed that the increasing cation disorder is responsible for the suppression of the long-range AFM order. Magnetic susceptibility measurements suggest the presence of ferromagnetic clusters in the paramagnetic region, and the formation of a spin-glass state at $T_f = 41$ K as a result of magnetic frustrations.

## ACKNOWLEDGMENTS

This work was partially supported by the Australian Research Council. The measurements at ISIS were supported by a beamtime allocation from the Science and Technology Facilities Council and by the Australian Research Council Grant "Access for Australian Researchers to Advanced Neutron Beam Techniques," Australian Institute of Nuclear Science and Engineering, and the Access to Major Research Facilities Program.

---

[*] zhaoming.zhang@ansto.gov.au

[1] R. von Helmolt, J. Wecker, B. Holzapfel, L. Schultz, and K. Samwer, Phys. Rev. Lett. **71**, 2331 (1993).

[2] K.-i. Chahara, T. Ohno, M. Kasai, and Y. Kozono, Appl. Phys. Lett. **63**, 1990 (1993).

[3] S. Jin, T. H. Tiefel, M. McCormack, R. A. Fastnacht, R. Ramesh, and L. H. Chen, Science **264**, 413 (1994).

[4] N. Mathur and P. Littlewood, Phys. Today **56**, 25 (2003).

[5] T. Negas and R. S. Roth, J. Solid State Chem. **1**, 409 (1970).

[6] H. Y. Wu, K. Q. Ruan, S. L. Huang, Z. M. Lv, and L. Z. Cao, Solid State Commun. **141**, 198 (2007).

[7] B. J. Kennedy, P. J. Saines, Q. D. Zhou, Z. M. Zhang, M. Matsuda, and M. Miyake, J. Solid State Chem. **181**, 2639 (2008).

[8] A. Sundaresan, J. L. Tholence, A. Maignan, C. Martin, M. Hervieu, B. Raveau, and E. Suard, Eur. Phys. J. B **14**, 431 (2000).

[9] H. Sakai, S. Ishiwata, D. Okuyama, A. Nakao, H. Nakao, Y. Murakami, Y. Taguchi, and Y. Tokura, Phys. Rev. B **82**, 180409 (2010).

[10] Z. M. Zhang, B. J. Kennedy, C. J. Howard, L. Y. Jang, K. S. Knight, M. Matsuda, and M. Miyake, J. Phys.: Condens. Matter **22**, 445401 (2010).

[11] P. Mandal, A. Hassen, and A. Loidl, Phys. Rev. B **69**, 224418 (2004).

[12] Z. Zeng, M. Greenblatt, and M. Croft, Phys. Rev. B **63**, 224410 (2001).

[13] W. J. Lu, B. C. Zhao, R. Ang, W. H. Song, J. J. Du, and Y. P. Sun, Solid State Commun. **136**, 196 (2005).

[14] W. J. Lu, B. C. Zhao, R. Ang, W. H. Song, J. J. Du, and Y. P. Sun, Phys. Lett. A **346**, 321 (2005).

[15] M. A. Carpenter, H. W. Meyer, P. Sondergeld, S. Marion, and K. S. Knight, Am. Mineral. **88**, 534 (2003).

[16] M. A. Carpenter, C. J. Howard, B. J. Kennedy, and K. S. Knight, Phys. Rev. B **72**, 024118 (2005).

[17] M. A. Carpenter, A. I. Becerro, and F. Seifert, Am. Mineral. **86**, 348 (2001).

[18] M. A. Carpenter, C. J. Howard, K. S. Knight, and Z. Zhang, J. Phys.: Condens. Matter **18**, 10725 (2006).

[19] C. J. Howard, Z. Zhang, M. A. Carpenter, and K. S. Knight, Phys. Rev. B **76**, 054108 (2007).

[20] E. K. H. Salje, *Phase transitions in ferroelastic and co-elastic crystals* (Cambridge University Press, Cambridge, 1993).

[21] M. A. Carpenter, E. K. H. Salje, and A. Graeme-Barber, Eur. J. Mineral. **10**, 621 (1998).

[22] R. M. Ibberson, W. I. F. David, and K. S. Knight, *The High Resolution Neutron Powder Diffractometer (HRPD) at ISIS—A User Guide, Report RAL 92-031* (Rutherford Appleton Laboratory, Didcot, 1992).

[23] Z. M. Zhang, C. J. Howard, K. S. Knight, and G. R. Lumpkin, Acta Crystallogr. B **62**, 60 (2006).

[24] H. M. Rietveld, J. Appl. Crystallogr. **2**, 65 (1969).

[25] A. C. Larson and R. B. von Dreele, *General Structure Analysis System (GSAS)*, *Report LAUR 86-748* (Los Alamos National Laboratory, Los Alamos, 1994).

[26] B. H. Toby, J. Appl. Crystallogr. **34**, 210 (2001).

[27] A. M. Glazer, Acta Crystallogr. B **28**, 3384 (1972).

[28] Z. M. Zhang, C. J. Howard, B. J. Kennedy, M. Matsuda, and M. Miyake, J. Phys.: Condens. Matter **21**, 124218 (2009).

[29] T. Proffen, R. G. DiFrancesco, S. J. L. Billinge, E. L. Brosha, and G. H. Kwei, Phys. Rev. B **60**, 9973 (1999).

[30] T.-Y. Tan, B. J. Kennedy, Q. Zhou, C. D. Ling, W. Miiller, C. J. Howard, M. A. Carpenter, and K. S. Knight, Phys. Rev. B **85**, 104107 (2012).

[31] R. D. Shannon, Acta Crystallogr. A **32**, 751 (1976).

[32] L. M. Rodriguez-Martinez and J. P. Attfield, Phys. Rev. B **54**, R15622 (1996).

[33] L. M. Rodriguez-Martinez and J. P. Attfield, Phys. Rev. B **58**, 2426 (1998).

[34] P. G. Radaelli, M. Marezio, H. Y. Hwang, and S. W. Cheong, J. Solid State Chem. **122**, 444 (1996).

[35] H. Y. Hwang, T. T. M. Palstra, S. W. Cheong, and B. Batlogg, Phys. Rev. B **52**, 15046 (1995).

[36] P. G. Radaelli, G. Iannone, M. Marezio, H. Y. Hwang, S. W. Cheong, J. D. Jorgensen, and D. N. Argyriou, Phys. Rev. B **56**, 8265 (1997).

[37] M. A. Carpenter and C. J. Howard, Acta Crystallogr. B **65**, 134 (2009).

[38] Z. M. Zhang, G. R. Lumpkin, C. J. Howard, K. S. Knight, K. R. Whittle, and K. Osaka, J. Solid State Chem. **180**, 1083 (2007).

[39] E. K. H. Salje, B. Wruck, and H. Thomas, Z. Phys. B: Condens. Matter **82**, 399 (1991).

[40] S. A. Hayward and E. K. H. Salje, J. Phys.: Condens. Matter **10**, 1421 (1998).

[41] B. J. Kennedy, C. J. Howard, and B. C. Chakoumakos, Phys. Rev. B **59**, 4023 (1999).

[42] B. J. Kennedy, C. J. Howard, and B. C. Chakoumakos, Phys. Rev. B **60**, 2972 (1999).

[43] S. A. Hayward, S. A. T. Redfern, and E. K. H. Salje, J. Phys.: Condens. Matter **14**, 10131 (2002).

[44] M. A. Carpenter, Am. Mineral. **92**, 309 (2007).

[45] M. A. Carpenter and C. J. Howard, Acta Crystallogr. B **65**, 147 (2009).

[46] B. J. Kennedy and Q. Zhou, Solid State Commun. **147**, 208 (2008).

[47] M. W. Lufaso, P. M. Woodward, and J. Goldberger, J. Solid State Chem. **177**, 1651 (2004).

[48] J. M. Kiat and T. Roisnel, J. Phys.: Condens. Matter **8**, 3471 (1996).

[49] B. J. Kennedy, A. K. Prodjosantoso, and C. J. Howard, J. Phys.: Condens. Matter **11**, 6319 (1999).

[50] C. N. W. Darlington, Phys. Status Solidi A **155**, 31 (1996).

[51] B. J. Kennedy, C. J. Howard, and B. C. Chakoumakos, J. Phys.: Condens. Matter **11**, 1479 (1999).

[52] B. J. Kennedy and B. A. Hunter, Phys. Rev. B **58**, 653 (1998).

[53] M. A. Carpenter, R. E. A. McKnight, C. J. Howard, Q. Zhou, B. J. Kennedy, and K. S. Knight, Phys. Rev. B **80**, 214101 (2009).

[54] A. G. Christy, Acta Crystallogr. B **51**, 753 (1995).

[55] M. C. Sánchez, G. Subías, J. García, and J. Blasco, Phys. Rev. Lett. **90**, 045503 (2003).

[56] X. Qiu, T. Proffen, J. F. Mitchell, and S. J. L. Billinge, Phys. Rev. Lett. **94**, 177203 (2005).

[57] J. C. Nie, J. H. Wang, and B. R. Zhao, J. Magn. Magn. Mater. **192**, L379 (1999).

[58] J. Topfer and J. B. Goodenough, J. Solid State Chem. **130**, 117 (1997).

[59] S. de Brion, F. Ciorcas, G. Chouteau, P. Lejay, P. Radaelli, and C. Chaillout, Phys. Rev. B **59**, 1304 (1999).

[60] J. A. Mydosh, *Spin Glasses* (Taylor & Francis, London, 1995).

[61] S. Hashimoto and H. Iwahara, J. Electroceram. **4**, 225 (2000).

[62] X. Fabreges, S. Petit, I. Mirebeau, S. Pailhes, L. Pinsard, A. Forget, M. T. Fernandez-Diaz, and F. Porcher, Phys. Rev. Lett. **103**, 067204 (2009).

[63] S. Shimomura, T. Tonegawa, K. Tajima, N. Wakabayashi, N. Ikeda, T. Shobu, Y. Noda, Y. Tomioka, and Y. Tokura, Phys. Rev. B **62**, 3875 (2000).

[64] C. Piamonteze, H. C. N. Tolentino, A. Y. Ramos, N. E. Massa, J. A. Alonso, M. J. Martínez-Lope, and M. T. Casais, Phys. Rev. B **71**, 012104 (2005).

[65] J. B. Goodenough, Phys. Rev. **117**, 1442 (1960).